JGR Atmospheres

RESEARCH ARTICLE
10.1029/2019JD032167

Surface and Atmospheric Driven Variability of the Single-Layer Urban Canopy Model Under Clear-Sky Conditions Over London

A. Tsiringakis[1], A. A. M. Holtslag[1], Sue Grimmond[2], and G. J. Steeneveld[1]

[1]Meteorology and Air Quality Section, Wageningen University & Research, Wageningen, The Netherlands, [2]Department of Meteorology, University of Reading, Reading, UK

Key Points:
- High daytime temperatures lead to increased nocturnal atmospheric stability and radiative cooling
- Nonlinear model response highlights the need to use coupled land-surface atmosphere models during sensitivity tests
- Differences in physical description can be explained via changes in atmospheric forcing or surface parameters

Supporting Information:
- Supporting Information S1

Correspondence to:
A. Tsiringakis,
aristofanis.tsiringakis@wur.nl

Citation:
Tsiringakis, A., Holtslag, A. A. M., Grimmond, S., & Steeneveld, G. J. (2020). Surface and atmospheric driven variability of the single-layer urban canopy model under clear-sky conditions over London. *Journal of Geophysical Research: Atmospheres*, *125*, e2019JD032167. https://doi.org/10.1029/2019JD032167

Received 2 DEC 2019
Accepted 7 JUN 2020
Accepted article online 19 JUN 2020

Abstract Urban canopy models (UCMs) are parametrization schemes that are used to improve weather forecasts in urban areas. The performance of UCMs depends on understanding potential uncertainty sources that can generally originate from the (a) urban surface parameters, (b) atmospheric forcing, and (c) physical description. Here, we investigate the relative importance of surface and atmospheric driven model sensitivities of the single-layer urban canopy model when fully interactive with a 1-D configuration of the Weather Research and Forecasting model (WRF). The impact of different physical descriptions in UCMs and other key parameterization schemes of WRF is considered. As a case study, we use a 54-hr period with clear-sky conditions over London. Our analysis is focused on the surface radiation and energy flux partitioning and the intensity of turbulent mixing. The impact of changes in atmospheric forcing and surface parameter values on model performance appears to be comparable in magnitude. The advection of potential temperature, aerosol optical depth, exchange coefficient and roughness length for heat, surface albedo, and the anthropogenic heat flux are the most influential. Some atmospheric forcing variations have similar impact on the key physical processes as changes in surface parameters. Hence, error compensation may occur if one optimizes model performance using a single variable or combinations that have potential for carryover effects (e.g., temperature). Process diagrams help differences to be understood in the physical description of different UCMs, boundary layer, and radiation schemes and between the model and the observations.

1. Introduction

Urban canopy models (UCM) are essential components of many numerical weather prediction (NWP) models as they represent subgrid scale physical process of the urban fabric. However, given their complexity, UCMs' performance is not always well understood. Large variations in model performance have been reported between different UCMs (Grimmond et al., 2010) with similar configurations for the urban surface parameters (Best & Grimmond, 2015; Grimmond et al., 2010) and between the same UCM with different configurations (Grimmond et al., 2010; Loridan et al., 2010).

One source of uncertainty in the performance of a UCM originates from the complexity of the representation of the urban surface in the UCM (Best & Grimmond, 2015). The complexity ranges from bulk schemes that only account for basic surface parameters to multilayer schemes accounting for building drag effects and street-canyon orientation (Jarvi et al., 2011; Kusaka et al., 2001; Martilli et al., 2002; Masson, 2000; Salamanca & Martilli, 2009). The simpler physical description in less complex UCMs could potentially lead to worse performance from incomplete representation of physical mechanisms in the urban environment.

Best and Grimmond (2015) showed that differences in complexity between UCM might not be the primary source of model bias. Their findings, supported also by those of Loridan et al. (2010), Demuzere et al. (2017), and Ronda et al. (2017), suggest that adequate prescription of urban surface parameters is equally essential (if not more) for reducing model biases. The surface parameters are also linked to key physical processes, like radiation absorption (e.g., surface albedo and emissivity) and surface energy partitioning. Given the plethora of parameters that are needed to be known, disentangling the contribution of each parameter on model performance can be time consuming (Loridan et al., 2010; Loridan & Grimmond, 2012; Zhao et al., 2014). An offline multioptimization that minimizes errors due to uncertainties in surface parameters in a UCM is possible (Loridan et al., 2010). However, understanding the contribution of all surface parameter changes to key

physical process in the urban fabric, and the coupling with the overlying atmosphere is virtually an impossible task.

Complexity increases further when UCMs are coupled to the atmosphere. In such cases an offline multioptimization approach might not have the expected improvement in model performance, as model response to changes in parameters setting varies substantially depending on whether a UCM is coupled to the atmosphere or not (Tsiringakis et al., 2019). However, when coupled to a NWP model, UCM uncertainty increases also from variations in atmospheric forcing provided by the different parameterization schemes coupled with the UCM. Ferrero et al. (2018) found that BEP and BEP + BEM models perform better when coupled to TKE-based boundary layer schemes. This highlights that the turbulent mixing intensity strongly affects model performance, through modification of near-surface atmospheric forcing. Such findings are also supported by Sterk et al. (2013) and Bosveld et al. (2014).

Therefore, it is not surprising that in-depth knowledge on UCM performance when coupled to NWPs is still limited. It is essential to know which uncertainty sources could have the largest impact on the key radiative, surface energy, and turbulent mixing processes. We investigate if different uncertainty sources have similar impacts on model variability to identify compensating effects on model bias. Changes in surface parameters and atmospheric forcing on three key physical process are tested. The results are utilized to identify why model performance varies between different UCMs coupled to the same NWP and between the same UCM coupled to different boundary layer and radiation schemes existing in the NWP model.

The impact of changes in surface parameters and atmospheric forcing on the surface radiation balance, surface flux partitioning, and turbulent mixing in the single-layer urban canopy model (SLUCM, Kusaka et al., 2001) coupled to the Weather Research and Forecasting (WRF) model (Powers et al., 2017; Skamarock et al., 2008) is studied using a case study (section 2). A brief evaluation with observations is conducted prior to an in-depth analysis of the model variability caused by changes in surface parameters and atmospheric forcing (section 3). We explore how physical processes modified by changes in the atmospheric forcing and surface parameters can explain variations between different parameterization schemes (section 4). Finally discussion and conclusions are drawn (sections 5and 6).

2. Methodology

2.1. Case Study Description

A clear-sky 54-hr period (00:00 UTC 23 July 2012 to 06:00 UTC 25 July 2012) from the SUBLIME study (Steeneveld et al., 2017; Tsiringakis et al., 2019) is used. A spin-up time of 6 hr is used to allow building temperatures adjust to the changes in atmospheric forcing components and surface parameters. The first 24-hr (06:00 UTC 23 July 2012 to 05:00 UTC 24 July 2012) are used for the primary focus of this paper (sections 3.2, 3.3, 3.4, and 4). For the following 24-hr (06:00 UTC 24 July 2012 to 05:00 UTC 25 July 2012) the sensitivity analyses are repeated. This latter material and comparison to the prior day is presented in the supporting information.

Observations taken at the King's College London measurement site (KSSW) (Kotthaus & Grimmond, 2014a, 2014b) include temperature, wind, radiation, and surface fluxes at 50 m above ground level (a.g.l.). The local urban surface properties used for the reference experiment (Table 1) are based on existing literature for the KSSW site (Kotthaus & Grimmond, 2014a, 2014b) and central London (Bohnenstengel et al., 2014b; Oikonomou et al., 2012). Other surface parameters used (not in Table 1) are (a) average building height, (b) aspect ratio, (c) roof width, (d) albedo, (e) heat capacity, (f) thermal conductivity, and (g) emissivity values for all facets. These are from SUBLIME (Steeneveld et al., 2017; Tsiringakis et al., 2019) and are available on the SUBLIME website (www.met.wur.nl/sublime).

The atmospheric forcing (Steeneveld et al., 2017; Tsiringakis et al., 2019) includes initial profiles for potential temperature, wind, mixing ratio (up to 17 km) and surface pressure. The 1-D WRF model initialization profiles are based on a radio-sounding (UWYO, 2012) at Herstmonceux, Hailsham, UK, at 00 UTC 23 July 2012 and are adjusted using the KSSW measurements and 3-D WRF model derived profiles over London. The adjustment with KSSW and 3-D WRF is done to ensure an accurate estimate of boundary temperature, moisture, and wind given the 70 km separation between KSSW and Herstmonceux.

Table 1
Experiment With Reference Values Held Constant When Another Parameter Is Varied Across the Uncertainty Range

Experiment name	Parameter	Reference	Values used
f_{urb}_value	f_{urban} (0–1)	0.85	0.75, 0.80, 0.85, 0.90, 0.95
α_{roof}_value	α_{roof} (0–1)	0.18	0.10, 0.15, 0.18, 0.25, 0.30
λ_{wall}_value	λ_{wall} (J s^{-1} K^{-1})	0.60	0.15, 0.45, 0.60, 0.75, 1.05
C_{wall}_value	C_{wall} (J m^{-3} K^{-1} $*10^6$)	1.50	0.60, 1.20, 1.50, 1.80, 2.40
a_{kanda}_value	a_{kanda} (−)	1.00	0.50, 0.80,1.00, 1.10, 1.40
Q_f_value	Q_f (W m^{-2})	38.0	10.0, 30.0, 38.0, 50.0, 70.0

Note. Experiment naming uses the surface parameters tested and their value. See Table A1 for notation definitions.

Boundary conditions for the 1-D WRF model are applied in the form of subsidence, geostrophic wind, and advection tendency terms for potential temperature, moisture, and u and v wind components. Geostrophic wind is derived from 6-hourly ECMWF operational reanalysis data (ECMWF, 2012) in combination with a 3-D WRF simulations (hourly data) (Steeneveld et al., 2017; Tsiringakis et al., 2019). Geostrophic wind values are given as 6-hourly means, with a tendency term applied to the u and v geostrophic wind components at each time step (of 1-D WRF) to ensure a smooth change in geostrophic wind through the 6-hourly blocks and avoid oscillations from imbalance between actual and geostrophic wind speeds.

Advection for potential temperature, mixing ratio and momentum (u and v wind) are imposed throughout the 54-hr period as additional tendency terms in the prognostic equations for the specified variables. These tendency terms are derived from 3-D WRF model simulations for London (Tsiringakis et al., 2019). The hourly advection terms from 3-D WRF are averaged with advection estimates from WMO stations (NOAA/NCDC, 2012) within and around London. Six-hourly means are obtained from the hourly values. Thus a static advection is prescribed (i.e., independent of the 1-D WRF temperatures) that changes every 6 hr in the 1-D WRF simulation. Advection is treated as uniform throughout the observed height of the boundary layer, with a sharp linear decrease above. This new approach is preferred to avoid daytime stable stratification from a sharp decrease of negative temperature advection between 500 and 1,500 m, as in the original SUBLIME forcing (Steeneveld et al., 2017; Tsiringakis et al., 2019). The latter affects the distribution of TKE in the upper part of the boundary layer, thus impacting the boundary layer height and the temperature and moisture profiles.

Initial soil temperature and moisture content profiles (to 1.5 m depth), surface temperature for vegetation and urban surfaces are provided. They are derived from a 3-D WRF simulation and then cycled 3×2 days in an offline setup, until the deepest soil temperature became constant and storage heat flux shows a similar diurnal range for both days of the case study (Tsiringakis et al., 2019).

2.2. Model Description and Setup

Here we use the single-column version of WRF v3.8.1 (Skamarock et al., 2008). The urban surface is parameterized based on the SLUCM scheme (Chen et al., 2011; Kusaka et al., 2001) with the Noah-LSM scheme (Chen & Dudhia, 2001) representing the vegetated land-surface processes. SLUCM separates the urban surface into three facets (roof, road, and wall), each with their distinct sky-view factor based on urban morphological parameters. The turbulent sensible heat (Q_H) flux from each facet is calculated:

$$Q_H = \rho\, c_P\, C_H\, U_a\, (\Delta\theta), \tag{1}$$

where ρ is the air density (kg m^{-3}), c_p is the specific heat capacity of dry air (J kg^{-1} K^{-1}), and C_H is the exchange coefficients for heat. $\Delta\theta$ (K) is the potential temperature difference between the surface and the air. U_a is the wind speed (m s^{-1}) at the first model level. The urban and vegetation fluxes are combined using a tiling approach based on their plan area fraction. The anthropogenic heat flux (Q_f) (added to the first model level) is prescribed with a diurnal cycle. For more details about SLUCM physical description and parameters see Loridan et al. (2010).

The surface layer and boundary layer are parameterized using Mellor-Yamada-Janjic (MYJ) schemes (Janjic, 1994). Radiative processes for long-wave and short-wave radiation are obtained from the RRTMG radiation

schemes (Iacono et al., 2008), while for microphysics the WSM 3-class order scheme (Hong et al., 2004) is used. The model uses 70 vertical levels that extent to 17 km, with 25 levels within the lowest 1.5 km.

2.3. Strategy for the Sensitivity Tests

Sensitivity tests are conducted to address the three sources of uncertainty influencing model performance: (a) surface parameters, (b) atmospheric forcing, and (c) the differences in physical description in other essential parameterization schemes. The aim is to identify the effects these have on the surface radiation, energy fluxes, and turbulent intensity.

2.3.1. Surface Parameters

Based on Loridan et al. (2010) and Zhao et al. (2014), we identify urban fraction (f_{urban}), albedo (a), thermal conductivity (λ), heat capacity (C), the a_{kanda} parameter, and the anthropogenic heat flux (Q_f) as the most influential surface parameters. Note that as Q_f is prescribed in SLUCM it is treated as a parameter rather than a variable. For simplicity we investigate only the impact of roof albedo (a_{roof}), wall thermal conductivity (λ_{wall}), and heat capacity (C_{wall}) rather than all facets. Tsiringakis et al. (2019) found these to have the dominant impact on model performance in the current model configuration.

The a_{kanda} parameter modifies the roughness length of heat (Zo_{hc}) from the one of momentum (Zo_{mc}) above the urban canyon and the overlying atmosphere (Kanda et al., 2007; Loridan et al., 2010) via,

$$Zo_{hc} = Zo_{mc} e^{\left(2 - a_{kanda} \left(Re_c^*\right)^{0.25}\right)}, \tag{2}$$

where Re_c^* is the Reynolds roughness number. Hence the a_{kanda} primarily influences the ratio between sensible (Q_H) and storage (ΔQ_s) heat fluxes, with larger values decreasing Q_H (and vice versa). It thus impacts the skin temperatures, surface flux partitioning, turbulent mixing in the surface layer, and the outgoing long-wave radiation (LW_U) due to lower ΔQ_s.

Q_f is a very uncertain parameter as in reality it is highly variable with strong dependence on anthropogenic activities (Bohnenstengel et al., 2014; Dong et al., 2017; Iamarino et al., 2012). For London values can vary between 10 and 140 W m^{-2}, depending on the location and area extent, with estimates reaching 200 W m^{-2} in central London (Iamarino et al., 2012) but small when averaged over larger areas (Dong et al., 2017; Lindberg et al., 2013). Ward et al. (2016) estimate Q_f for this study area to vary temporally between 20 and 80 W m^{-2}. Considering how important the anthropogenic heat flux can be for the surface energy balance (Best & Grimmond, 2016) it is essential to include it in our analysis. Reference values, incremental change, and minimum/maximum variation limits for the surface parameters (Table 1) are based on Dong et al. (2017), Iamarino et al. (2012), Loridan et al. (2010), Ward et al. (2016), Zhao et al. (2014), and Tsiringakis et al. (2019).

2.3.2. Atmospheric Forcing

The atmospheric effects investigated are the impact of radiation, advection of heat and moisture, and turbulent mixing intensity. Short-wave radiation biases in cities are common even in clear-sky conditions (Tsiringakis et al., 2019) by WRF, especially due to aerosol loading effects on direct short-wave radiation (Gomes et al., 2008; Kokkonen et al., 2019). Hence we modulate the aerosol optical depth (AOD) to simulate effects on radiation between clearer and more polluted atmospheric conditions. Terra/MODIS satellite derived AOD (Levy et al., 2013) range between 0.1 and 0.4 (0.18 in the reference run) depending on the distance from central London and the timing of the measurement (NASA/EOSDIS, 2019). Long-wave radiation biases in models participated in GABLS (including WRF) (Bosveld et al., 2014; Kleczek et al., 2014) suggest that long-wave downward radiation (LW_D) biases are caused by bias in boundary layer temperature and humidity and different physical complexity of the radiation models. Using an extreme CO_2 uncertainty range (38–3,800 ppm) we increase and decrease the long-wave downward (LW_D) radiation without changing directly air temperature or humidity. This allows us to further disentangle the atmospheric driven uncertainty in LW_D from the physical driven one.

Heat (ADV_θ) and moisture (ADV_q) advection are inherently difficult to estimate correctly especially in heterogeneous environments. Yet they strongly impact the near-surface temperature and the surface energy balance (Heaviside et al., 2015). ADV_θ and ADV_q forcing are both positive and negative in the study period. Multiplication factors (Table 2) are applied to the negative advection values. Positive advection

Table 2
As Table 1 but for Atmospheric Forcing

Experiment	Atmospheric forcing	Reference	Values used
AOD_value	*AOD* (0–1)	0.18	0.00, 0.09, 0.18, 0.27, 0.36
CO_2*_value*	CO_2 (ppm)	380	38, 76, 380, 1900, 3800
CH_{heat}*_value*	CH_{heat} (mult. factor)	1.00	0.67, 0.80, 1.00, 1.25, 1.50
CH_{mom}*_value*	CH_{mom} (mult. factor)	1.00	0.67, 0.80, 1.00, 1.25, 1.50
ADV_θ*_value*	ADV_θ (mult. factor)	1.00	0.67, 0.80, 1.00, 1.25, 1.50
ADV_q*_value*	ADV_q (mult. factor)	1.00	0.67, 0.80, 1.00, 1.25, 1.50

Note. Aerosol optical depth (AOD) and CO_2 concentration values change, whereas the remainder use a multiplication factor.

values receive the inverse multiplication factor for these tests (e.g., when $ADV_\theta < 0$ values are multiplied by 1.25, positive values are multiplied by 0.8 and vice versa).

To investigate the impact of turbulent mixing intensity we modify the exchange coefficients for heat (CH_{heat}) and momentum (CH_{mom}) for the urban, surface layer, and boundary layer schemes. These coefficients are linearly (Table 2) enhanced or decreased to modify the coupling between the surface and overlying atmosphere. The turbulent mixing impacts the performance of the surface layer scheme (Bosveld et al., 2014; Sterk et al., 2013) and can explain much of the biases (i.e., long-wave radiation, near-surface temperature, and surface energy fluxes) between model results and observations. Here we investigate fully convective boundary layers, whereas previously neutral and stable boundary layers have been studied. Hence our range of the multiplication factors for the exchange coefficients (0.67–1.50) is smaller than that used by Sterk et al. (2013) and Bosveld et al. (2014) (0.25–4).

2.3.3. Physical Ensemble Tests

Variability in model performance is also caused by the model physics used to parameterize subgrid scale processes. The PILPS urban (Grimmond et al., 2010, 2011) and the GABLS (Bosveld et al., 2014; Kleczek et al., 2014) studies have investigated this variability in model performance for different UCMs, boundary layer, and surface layer schemes. Using different NWP models (as seen in GABLS) complicates the analysis of model differences, as physics schemes also vary, thus adding uncertainty.

Using WRF, we can vary the individual physics schemes, while keeping others unchanged giving us a "physical ensemble" that enables us to test the third source of uncertainty (physics description). Here we consider the radiative transfer, boundary layer, and UCM schemes available in WRF (Table 3).

For the urban surface, BEP and BEP + BEM multilayer urban canopy models are tested (Martilli et al., 2002; Salamanca & Martilli, 2009) with SLUCM (Kusaka et al., 2001) being the reference choice. For the boundary layer we test the Yonsei University scheme (YSU) Hong et al. (2006) and Quasinormal Scale Elimination (QNSE) Scheme (Sukoriansky et al., 2005) both coupled to WRF-SLUCM-Noah setup. The radiation scheme is changed to the CAM short-wave and long-wave radiation schemes (Collins et al., 2004).

2.4. Analysis of Process Diagrams

Process diagrams (Bosveld et al., 2014; Sterk et al., 2013) allow the impact of atmospheric forcing, surface parameters, or parameterization schemes changes to be explored relative to a control run for a pair of variables. Each model run is represented by the mean of the two variables under investigation for a specified period (e.g., daytime or nighttime). We link these points to identify if the response is linear or nonlinear. Model sensitivity tests allow identification of the dominant influences on the pair of variables under investigation, within the ranges of the perturbed parameters and atmospheric forcing components (Tables 1, 2, and 3). The mean observations are shown to help explain differences between model and observations. Following Bosveld et al. (2014) we use four perturbations and the reference model run to capture changes in parameters and atmospheric forcing components (including drawing the sensitivity lines), but we only show the maximum and minimum limits as points in the figures.

Table 3
Parameterization Schemes Varied From the Reference Setup in Seven Runs

Run	SW radiation	LW radiation	Boundary layer	UCM
R1(reference)	RRTMG	RRTMG	MYJ	SLUCM
R2	CAM	—	—	—
R3	—	CAM	—	—
R4	—	—	YSU	—
R5	—	—	QNSE	—
R6	—	—	—	BEP
R7	—	—	—	BEP + BEM

Note. Acronyms are explained in Appendix A1.

Sterk et al. (2013) and Bosveld et al. (2014) suggest that it is essential to identify variables combinations that are coupled/interdependent and are linked to the physical processes under investigation. Given the observations available we focus on (a) surface radiation balance, (b) surface energy flux partitioning, and (c) turbulent mixing separated by the time of day (based on surface net radiation Q^*) into day ($Q^* > 0\ \mathrm{W\,m^{-2}}$) and night ($Q^* < 0\ \mathrm{W\,m^{-2}}$) (Best & Grimmond, 2015), allowing the analysis of results under strong and weaker turbulent mixing regimes, when different physical processes dominate.

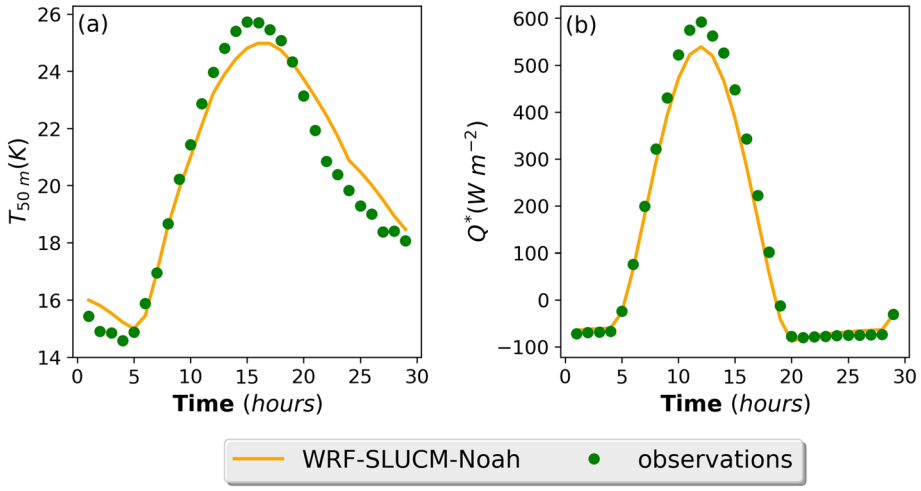

Figure 1. Modeled (reference setup) and observed hourly (a) air temperature (°C) and (b) net all-wave radiation (Q^*) (W m^{-2}) at 50 m above ground level at the KSSW site for the period 01:00 UTC 23 July 2012 to 06:00 UTC 24 July 2012.

3. Results

3.1. Model Evaluation for the Reference Model Setup

Here we briefly evaluate the 50 m air temperature and net all-wave radiation (Q^*). For a more extensive evaluation see Tsiringakis et al. (2019).

For the entire evaluation period (06:00 UTC 23 to 06:00 UTC 24 July) the reference run (R1) has a mean bias error (*MBE*) of 0.11°C (Figure 1). The modeled T_{50m} is cooler during daytime (*MBE* = −0.55°C) and warmer at night (*MBE* = 0.90°C) compared to the observations, suggesting the simulated temperature range is important. Therefore, the changes in temperature ($\Delta T_{50m} = T_{50m,max} - T_{50m,min}$) during daytime and nighttime is also considered. The observed daytime ΔT_{50m} is 9.85°C and 9.52°C when modeled (Figures 1 and 3). A nighttime *MBE* of 0.75°C exists between the modeled ΔT_{50m} (6.26°C) and observed (7.01°C).

For Q^* the reference run model has an *MBE* of −23.3 W m^{-2} originating from −43.6 W m^{-2} day *MBE* and a 0.7 W m^{-2} night. The daytime bias originates from short-wave downward radiation SW_D (*MBE* = 14.3 W m^{-2}), short-wave upward radiation SW_U (*MBE* = 24.8 W m^{-2}), long-wave downward radiation LW_D (*MBE* = −16.1 W m^{-2}) and long-wave upward radiation LW_U (*MBE* = 20.9 W m^{-2}) (Figure S1) biases. The nocturnal bias in Q^* originates from LW_D and LW_U biases of −8.1 and −8.8 W m^{-2}, respectively.

3.2. Surface Radiation Balance

From the sensitivity analyses the bias in SW_D is caused by aerosol optical depth (AOD), as all other parameter changes do not decrease SW_D. An AOD of 0.27 reduces the bias in SW_D. Terra/MODIS AOD data (Levy et al., 2013) for the study period (not shown) indicate a sharp increase of AOD from 0.15 (outskirts of London) to 0.25 (central business district, CBD). However, improving the SW_D estimate increases Q^* *MBE* (to −52 W m^{-2}) and net short-wave (S^*) at the surface. As the bias originates primarily from SW_U, we can attribute this to the bulk albedo of the urban surface. By decreasing a_{roof} to 0.12 we decrease the surface albedo (Figure 2b) and reduce the Q^* *MBE* (to −40 W m^{-2}). The bias in bulk albedo originates from the 2-D canyon physical description in SLUCM (Tsiringakis et al., 2019).

The remaining bias in Q^* is from the net long-wave radiation (L^*). The daytime bias in the LW_D is only partially explained by uncertainty in ADV_θ and ADV_q (~4–5 W m^{-2}, Table 4a). Large changes in CO_2, not supported by observational data, would be sufficient to account for this bias. However, it is more likely that the bias originates from a negative bias in mid-to-upper boundary layer temperature and moisture, but this cannot be verified with the existing observations. The LW_U biases are attributed to four different sources (CH_{heat}, a_{kanda}, c_{wall}, and λ_{wall}), with the first two being the stronger contributors. CH_{heat} and a_{kanda} alter

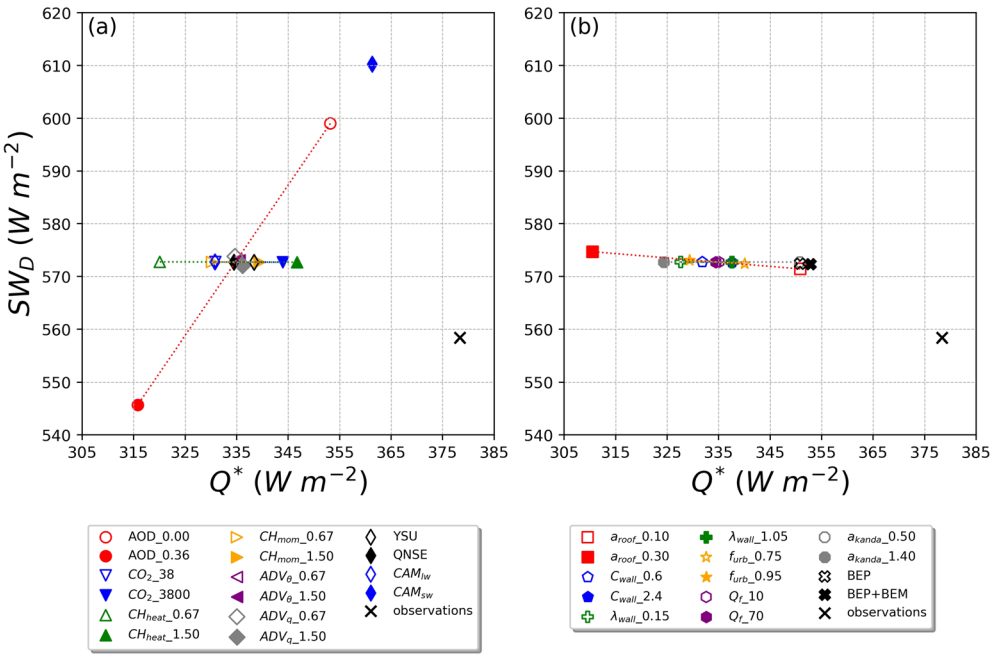

Figure 2. Sensitivity analysis across modeled uncertainty ranges (Tables 1, 2, and 3). Impact on the average SW_D and Q^* with changes in (a) atmospheric forcing, boundary layer, and radiation schemes and (b) changes in surface parameters and UCMs for daytime (06:00 UTC 23 July 2012 to 18:00 UTC 23 July 2012). For surface parameter (Table 1) and atmospheric forcing components (Table 2) only model runs using minimum (open symbol) and maximum (filled symbol) limit of the uncertainty range are shown, with lines between through all five runs.

Q^* by modulating the LW_U radiation via changes in skin temperature, with larger values for CH_{heat} (and lower for a_{kanda}) removing heat faster from the surface and thus reducing skin temperatures and LW_U.

While correcting the bias in Q^* is arbitrary, it does not lead to better model performance in general. The response of ΔT_{50m} for a given change in Q^* strongly depends on which atmospheric forcing or surface parameter is modified (Figure 3).

During the day, changes in ADV_θ have small effect in Q^*, but strongly impact ΔT_{50m} (1.8 K difference). The lack of variability in Q^* is from compensating changes in LW_D and LW_U (Table 4a) indicating that the boundary layer is in radiative balance with the surface, despite the drastic temperature change. An opposite effect is observed for changes in AOD, where the large decrease in Q^* (up to -37 W m^{-2} from 0 to 0.36 AOD) are not followed by a change in ΔT_{50m}. This is caused by the increase in radiative heating due to SW_D absorption at higher aerosol concentrations, which compensates for the decrease of air temperature by decreasing Q_H. Changes in CH_{heat} and CH_{mom} have positive Q^*−ΔT_{50m} relations with strong radiative heating at higher Q^* and vice versa (Figures 3a, 3b, S7a, and S8a). The change in ΔT_{50m} can be attributed to the changes in Q_H, which are caused by the changes in CH_{heat} (Equation 2).

Variations in SLUCM surface parameters have different impacts. Changes in a_{roof} and a_{kanda}, like CH_{heat} and CH_{mom}, have a positive trend (Figures 3b, S3a, S7a, and S8a), with a_{roof} having larger impact on Q^* (up to 40.4 Wm^{-2}), whereas a_{kanda} has more impact on ΔT_{50m}. The a_{roof} and a_{kanda} increase Q^* (and consequently Q_H), thus increasing ΔT_{50m} as well. However the effect of a_{kanda} on Q_H is also from changes in the roughness length of heat (Equation 1), which also impact the exchange coefficient of heat (Equation 2).

The effects of changing f_{urban},C_{wall}, and λ_{wall} cause an increase in ΔT_{50m} with a decrease in Q^* (Figure 3b). LW_u increases with smaller C_{wall}, λ_{wall}, and larger f_{urban} values (Table 4a). ΔT_{50m} increases with decreasing C_{wall} and λ_{wall} as ΔQ_s is decreased, hence increasing Q_H, while increasing f_{urban} changes the vegetation fraction, thus decreasing the Q_E and consequently increasing Q_H. Changes in Q_f and ADV_θ both have the same orientation (Figures 3a and 3b) but different magnitude, with Q_f not really affecting ΔT_{50m} during the daytime.

Table 4
Difference (δ) in Average Q^*, SW_D, LW_D, SW_U, LW_U, ΔT_{50m}, ΔT_{skin}, and q_{50m} for a Change Between the Maximum and Minimum Limits (Tables 1 and 2) for the Atmospheric Forcing and the Urban Surface Parameters for (a) Day ($Q^* > 0$) and (b) Night ($Q^* < 0$)

Parameters	δQ^*	δSW_D	δLW_D	δSW_U	δLW_U	$\delta(\Delta T_{50m})$	$\delta(\Delta T_{skin})$	δq_{50m}
(a) Day			W m^{-2}				K	g kg^{-1}
AOD (0–0.36)	−37.4	−53.3	−0.7	−8.2	−8.4	0.01	−0.31	0.09
CO_2 (38–3,800)	13.1	0.0	19.1	0.0	6.0	−0.11	−0.25	−0.07
CH_{heat} (0.67–1.5)	26.6	0.0	0.9	0.0	−25.8	0.86	−5.77	−0.20
CH_{mom} (0.67–1.5)	9.2	0.0	0.7	0.0	−8.5	0.56	−1.83	−0.03
ADV_θ (0.67–1.5)	−0.6	0.0	5.0	0.0	5.6	−1.76	−0.50	−0.14
ADV_q (0.67–1.5)	1.5	−1.7	3.9	−0.3	0.9	0.06	−0.05	0.94
a_{roof} (0.10–0.30)	−40.4	3.2	−2.4	53.2	−12.0	−0.98	−1.79	0.17
c_{wall} (0.60–2.4)	5.7	0.0	−0.5	0.0	−6.3	−0.58	−1.68	0.00
λ_{wall} (0.15–1.05)	10.0	0.0	−0.8	0.0	−10.8	−1.39	−3.00	0.01
f_{urban} (0.75–0.95)	−10.8	0.6	0.0	−0.9	12.3	0.59	2.49	0.51
Q_f (10–70)	−0.6	0.0	3.4	0.0	4.0	0.19	0.05	−0.21
a_{kanda} (0.50–1.40)	−26.4	0.0	−3.2	0.0	23.2	−1.83	5.29	0.23
(b) Night								
AOD (0–0.36)	−0.9	−3.8	−1.1	−0.6	−3.3	0.14	−1.02	0.10
CO_2 (38–3,800)	10.4	0.0	20.1	0.0	9.7	−0.65	−0.96	−0.03
CH_{heat} (0.67–1.5)	0.7	0.0	−0.7	0.0	−1.4	1.32	−2.12	−0.16
CH_{mom} (0.67–1.5)	0.2	0.0	−0.11	0.0	−0.3	0.61	−0.57	−0.01
ADV_θ (0.67–1.5)	2.3	0.0	−13.3	0.0	−10.9	0.45	0.06	−0.21
ADV_q (0.67–1.5)	4.9	−0.11	8.9	0.0	3.9	−0.22	−0.60	1.96
a_{roof} (0.10–0.30)	0.1	0.1	−3.2	1.0	−4.3	−0.25	−0.95	0.24
c_{wall} (0.60–2.4)	−2.4	0.0	0.1	0.0	2.5	−0.66	−1.80	0.04
λ_{wall} (0.15–1.05)	−1.6	0.0	−1.1	0.0	0.5	−0.45	−1.35	0.07
f_{urban} (0.75–0.95)	−7.5	0.0	0.6	0.0	8.1	−0.14	0.75	−0.87
Q_f (10–70)	−0.2	0.0	7.9	0.0	8.2	−1.39	−0.73	−0.25
a_{kanda} (0. 50–1.40)	−2.6	0.0	−2.0	0.0	0.6	−1.46	1.55	0.36

At night changes in ADV_θ, ADV_q, and CO_2 impact both Q^* and ΔT_{50m} (Figure 3c). However, changes in ADV_θ influence ΔT_{50m} more, while ADV_q mostly affects Q^*, by increasing LW_D radiation due to more water vapor in the boundary layer. The prescribed CO_2 concentration changes result in substantial changes in nocturnal Q^* (>10 W m^{-2}) and ΔT_{50m}. Increasing CH_{heat} and CH_{mom} result in an increase in ΔT_{50m} at night, which counteracts the daytime CH_{heat} effects (Tables 4a, 4b, and Figure S8). The increase in nighttime ΔT_{50m} is due to a decrease in daytime ΔQ_s (Figure 4a), which leads to smaller release of heat during the night (Figure 5a) and thus more radiative cooling. Consequently nocturnal air temperatures are lower in experiments with high CH_{heat} (Figure S8).

Changes in Q_f and a_{kanda} strongly influence nocturnal ΔT_{50m} (similar to CH_{heat}) but cause minimal variation in Q^*, given the radiative balance between LW_U and LW_D (Figure 3c and Table 4b). Increasing a_{kanda} leads to a small decrease in nocturnal Q^* due to the decrease in LW_D, a result of the lower air temperature due to less Q_H during the day. C_{wall} and λ_{wall} have a nonlinear behavior at nighttime, because of heat saturation effects of the urban fabric (Tsiringakis et al., 2019, and section 3.3). Both have a large impact on nocturnal ΔT_{50m} but also small effect (up to 3 W m^{-2}) on Q^*. Increasing f_{urban} results in the same decrease in Q^* from higher LW_U but only a minor decrease in ΔT_{50m}. This suggests that nighttime cooling rates surprisingly do not show a strong response to changes in f_{urban}. This can be explained by the strength of nocturnal radiative cooling. As discussed section S2.2, the increase in mean daytime air temperature due to higher f_{urban} leads to similar (or even stronger) cooling during the night (Figures S6d, S8a, and S8b). This nonlinear feedback involves an increase in daytime T_{50m} followed by an increase in nighttime surface to air temperature gradient, thus leading to stronger atmospheric stability and more radiative cooling (Figures S7–S10). Changes in f_{urban} are not the only triggering mechanism. It exists for most surface parameters and atmospheric forcing components that we investigated. Its impact is largest with lower wind speeds during the second day of the case study (section S2.3).

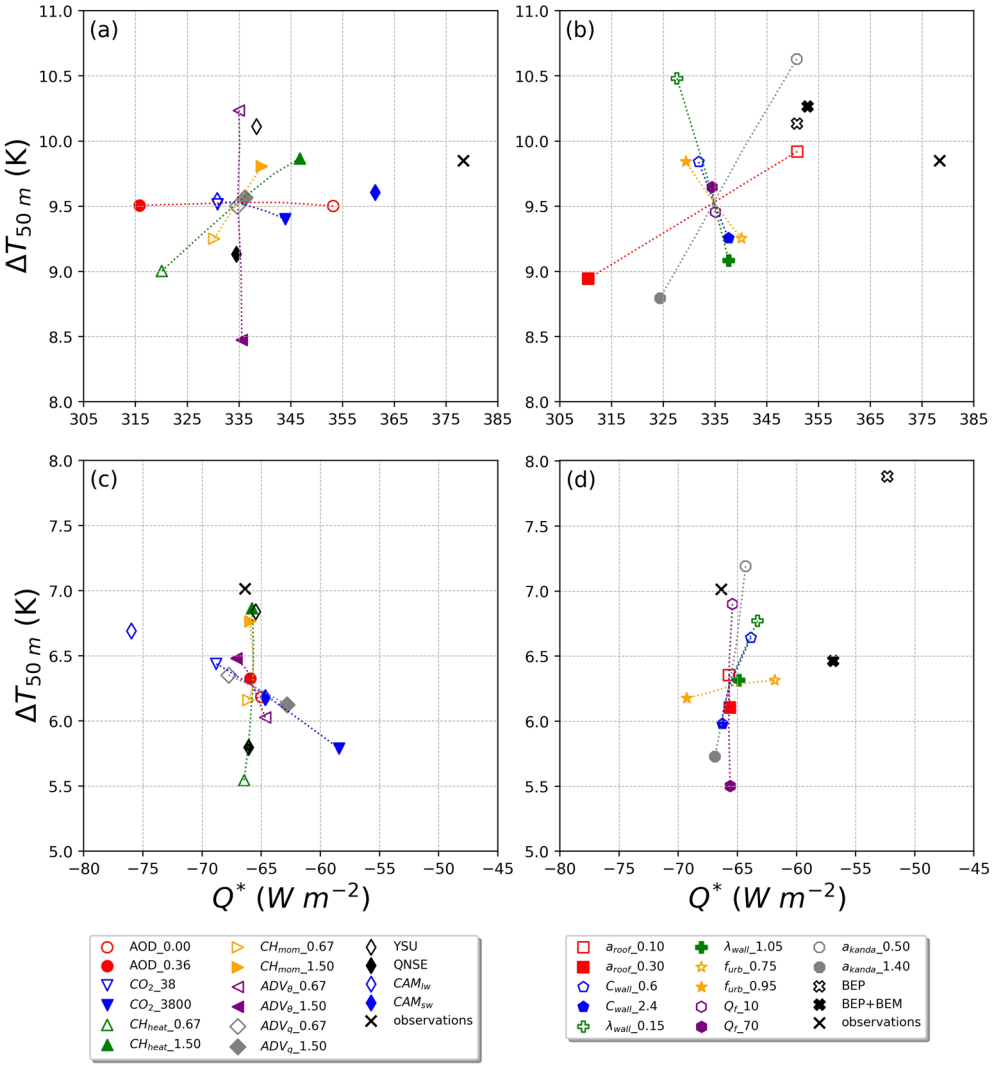

Figure 3. As Figure 2, but for the impact on change in 50 m air temperature ($\Delta T_{50m} = T_{50m,\,max} - T_{50m,\,min}$) and Q^* with changes in (a and c) atmospheric forcing, boundary layer, and radiation schemes and (b, d) in surface parameters and UCMs during (a, b) daytime (06:00 UTC 23 July 2012 to 18:00 UTC 23 July 2012) and (c, d) nighttime (19:00 UTC 23 July 2012 to 05:00 UTC 24 July 2012).

For the radiative balance and its effects on radiative heating and cooling, we find five sources of uncertainty in this case study accounting for a large part of the bias between model and observations. As discussed, correcting AOD and a_{roof} can explain the bias net-short-wave radiation and some of the bias in daytime ΔT_{50m}. Decreasing a_{kanda} and increasing CH_{heat} effectively removes heat faster from the urban surface, thus decreasing skin temperature and LW_U flux, while increasing ΔT_{50m} in both day and night. Finally a small increasing in the intensity of ADV_θ can compensate the ΔT_{50m} during the day. Some bias still remains in Q^* and is primarily associated with the bias in LW_D and some remaining bias in LW_U.

3.3. Energy Partitioning

Analysis of the surface energy partitioning is essential to understand the overall impact on atmospheric forcing and surface parameter changes in $\Delta T_{50\mathrm{m}}$. It provides further insight in compensating effects between day and night.

Regarding changes in atmospheric forcing during the daytime, AOD and CO_2 effectively maintain the same energy partitioning ratio (1.55 to 1.59) for both positive and negative changes in Q^*.

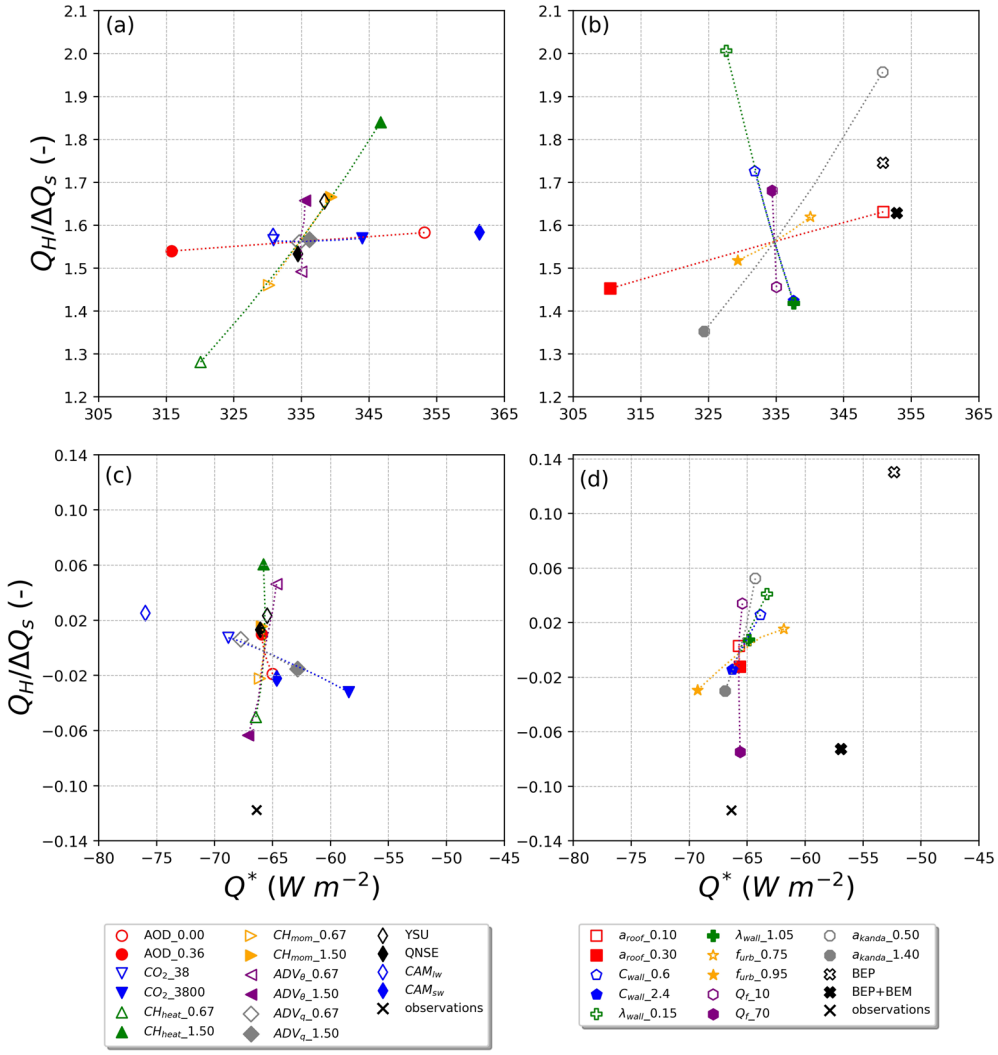

Figure 4. As Figure 3, but for the average surface flux ratio ($Q_H/\Delta Q_s$) and net radiation Q^*.

Consequently any energy gain or loss at the surface is distributed equally between the Q_H and ΔQ_s fluxes (Figure 4a). Changes in CH_{heat} and CH_{mom} impose a variation in energy partitioning, with lower values leading to faster decrease in Q_H and increase in ΔQ_s. The variation here is primarily caused by the response of Q_H due to changes in CH_{heat} (Equation 2). Q_E also decreases, but the flux variation from changes in CH_{heat} is an order of magnitude smaller than for Q_H (5 vs. 40 W m^{-2}). The decrease in Q_H results in less heat directed toward the atmosphere and more heat stored in the urban fabric, thus decreasing Q^* because of lower LW_D and larger LW_U (Table 4a). Changing advection has similar effects, but with lower variation in energy partitioning and no effect on Q^* due to the net long-wave radiative compensation.

Surface parameter changes have a wider impact in the parameter space (Figure 4b) compared to the change in atmospheric forcing, for the current choice of uncertainty range. Decreasing a_{roof} increases the $Q_H/\Delta Q_s$ flux ratio, with faster increase in Q_H compared to ΔQ_s due to thermal saturation effect on the roof facet. Thus, for the same change in Q^* there is a larger variability in ΔT_{50m} compared to changes in AOD (Figure 3b). Changes in a_{kanda} have a nearly identical response as CH_{heat} for the same reasons. The same occurs for changes in Q_f and ADV_θ, but despite their similar response in Q^* and energy partitioning, each parameter affects the ΔT_{50m} differently during the day and night. C_{wall} and λ_{wall} increase the $Q_H/\Delta Q_s$ ratio with decreasing parameter values due to higher skin temperature and higher LW_U.

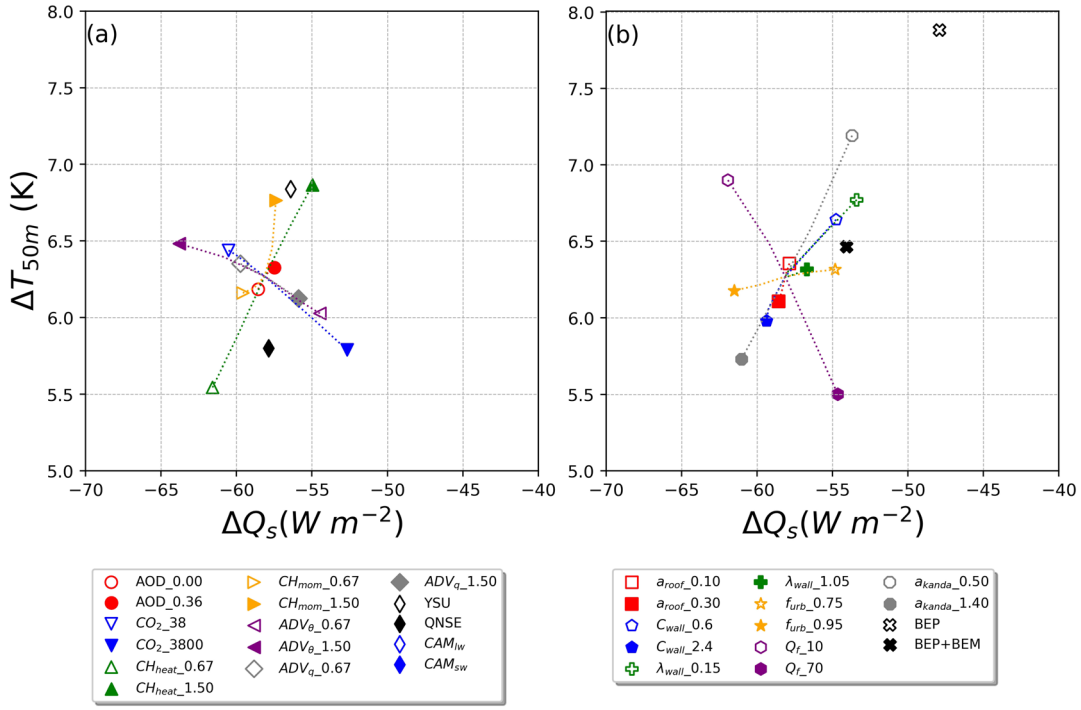

Figure 5. As Figure 2, but for change in (ΔT_{50m}) and the average storage heat flux (ΔQ_s) during nighttime (19:00 UTC 23 July 2012 to 05:00 UTC 24 July 2012).

Although some atmospheric forcing (CH_{heat} and CH_{mom}) and surface parameters (C_{wall} and λ_{wall}) cause a large variation in flux ratio and ΔT_{50m}, their impact on T_{50m} is small. This can be explained by the opposite effects on T_{50m} between night and day (Figure S8). For instance an increase in CH_{heat} leads to an increase in Q_H during the day but also decreases Q_H at nighttime (Figures 4a and 4c). Figure 5 shows that heat supply from the urban fabric at night is lower due to less ΔQ_s stored during the day as a result of the increase in CH_{heat}. These compensating effects are what limits the change in T_{50m}. Whereas parameters like Q_f and ADV_θ have smaller variations in the $Q_H/\Delta Q_s$ flux ratio but have strong impact on ΔT_{50m} both during day (ADV_θ) or night (Q_f). Hence, both affect the day and nighttime T_{50m} due to strong effects on their temperature that propagate from day to night and vice versa (Figures S8 and S9).

Following Tsiringakis et al. (2019) we do not derive the storage heat as the residual of surface energy balance, because of the accumulation of errors (Grimmond & Oke, 1999) and mismatch between the measurement footprint of the turbulent fluxes and the radiation fluxes (Schmid et al., 1991). Thus, we do not derive observed flux ratio during the day. However, the nocturnal $Q_H/\Delta Q_s$ ratio is strongly impacted by the sign and value of Q_H, given the difference between modeled (0.15 W m^{-2}) and observed (8.74 W m^{-2}) nocturnal Q_H, and the plausible range of nocturnal ΔQ_s (−50 to −100 W m^{-2}). At nighttime we use the objective hysteresis model (Grimmond & Oke, 1991) with the same coefficients as Ward et al. (2016) for this site forced by the observed Q^* to derive an "observed" nocturnal ΔQ_s (−74.3 W m^{-2}), leading to an "observed" $Q_H/\Delta Q_s$ estimate of −0.12. Although this is not an observation it allows exploration of how atmospheric forcing or surface parameters might explain the bias between model and observations.

At night the Q^* bias between model and observations is small (3 W m^{-2}), but the flux ratio is much smaller in the model because Q_H is nearly zero at night in the reference run. Increasing ADV_θ and Q_f or decreasing CH_{heat} and a_{kanda} can decrease the nighttime bias in the flux ratio. However, none can consistently correct biases in $Q_H/\Delta Q_s$ and ΔT_{50m} at the same time.

3.4. Intensity of Turbulent Mixing

The intensity of turbulent mixing, indicated by the bulk Richardson (Ri_b) number (between the 1st and 2nd model levels) aids in understanding the coupling between the urban surface and the overlying boundary

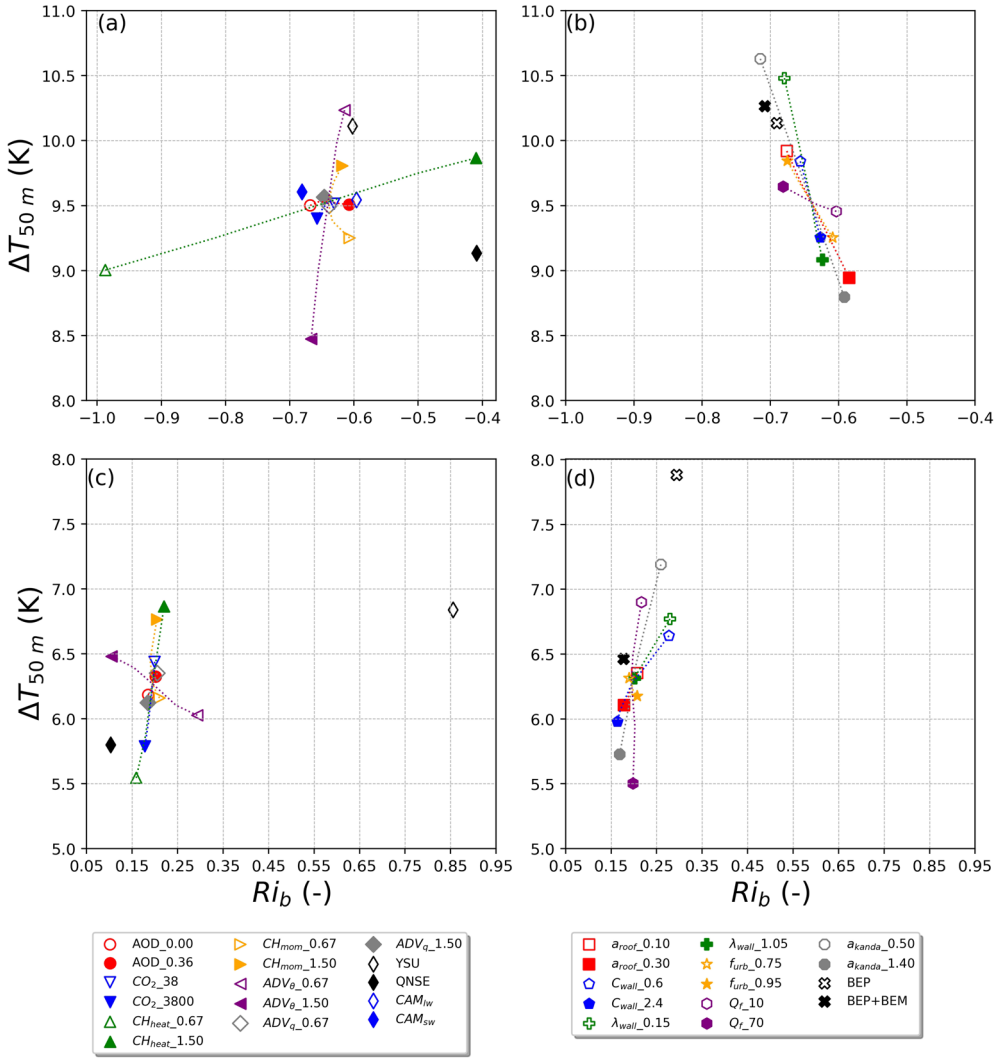

Figure 6. As Figure 3, but for changes in 50 m air temperature (ΔT_{50m}) and the average bulk Richardson number Ri_b.

layer. This can help us understand how the changes in the flux partitioning affect this coupling and how is this translated to the changes we identify in ΔT_{50m}.

Most of the changes in atmospheric forcing (Figure 6a) and surface parameters (Figure 6b) limit the variability of the Ri_b between −0.71 to −0.58 during the day, with daytime changes in AOD, CO_2 and ADV_q having small impact on Ri_b, and minimal effect in ΔT_{50m}. However, CH_{heat} causes large changes in Ri_b and ΔT_{50m}. Smaller increase ΔT_{50m} occurs at lower Ri_b values and weaker turbulent intensity, while the opposite is true for higher Ri_b values. This is somewhat counter-intuitive, because an increase in Q_H with larger values CH_{heat} would have increase the turbulent intensity and ΔT_{50m}. However, the increase in CH_{heat} results in heat being transported more rapidly from the surface into the boundary layer, warming up the entire boundary layer and reducing the temperature gradient near the surface, driving Q_H and Ri_b down during the day (Figure S10). Changes in ADV_θ cause a small decrease in Ri_b for an increasing in ΔT_{50m} (Figures 6a, S6a, and S6b). This is primarily caused by the increase in near-surface temperature gradient as colder air is advected above the warm surface.

Surface parameter changes show a clear influence on the ΔT_{50m}–Ri_b variable space, with a 0.2°C to 2.5°C change in ΔT_{50m} for a 0.1 change in Ri_b (Figure 6b). The a_{kanda}, a_{roof}, and Q_f have the largest impact on Ri_b during the day. These changes in Ri_b and ΔT_{50m} primarily originate from a change in Q_H.

At night (Figure 6c) ADV_θ, CO_2, and CH_{heat} show the largest impact on Ri_b and ΔT_{50m}. Changes in ADV_θ cause an increased ΔT_{50m} for weaker stability near the surface (smaller Ri_b). The decrease in atmospheric stability is caused by the decrease in near-surface temperature gradient, from the faster decrease in T_{50m} compared to changes in skin temperature, when strong negative ADV_θ is applied (Table 4b). This response when ADV_θ increases is from a stability feedback mechanism. This results in less radiative cooling and weaker atmospheric stability when daytime ΔT_{50m} decreases. Under low wind conditions, the impact of the feedback mechanisms intensifies and results in lower nocturnal ΔT_{50m} compared to the reference run (Figure S6c). The remaining atmospheric forcing modification or surface parameter changes shows an increase in nocturnal cooling rate, coinciding with also a faster heating rate during the day. Strong radiative cooling after sunset is the main driver for the stronger atmospheric stability in the experiment runs at night (Figures 6c and 6d).

Nocturnal surface parameter changes have a large impact on Ri_b and ΔT_{50m}, with changes in Q_f and λ_{wall} showing nonlinear responses during the night. Changes in C_{wall},λ_{wall}, and a_{kanda} have a strong impact in ΔT_{50m}, which compensates for the larger daytime increase in ΔT_{50m} (Figures 6b and 6d). This compensation leads to similar nighttime T_{50m} for these surface parameters (Figure S8a). Nocturnal ΔT_{50m} is strongly dependent on the radiative cooling and the atmospheric stability near the surface; thus surface parameters which increase daytime ΔT_{50m} result in stronger stability during the night. These findings support our hypothesis that a negative feedback mechanism exists between daytime ΔT_{50m} and nocturnal ΔT_{50m}.

4. Physical Ensemble Analysis

4.1. Radiation Schemes

Using the CAM short-wave radiation scheme, instead of the reference RRTMG, increases the SW_D bias to 51 W m^{-2}, while reducing the Q^* bias to −17 W m^{-2} (Figure 2a). The difference between the schemes aligns with the changes in AOD, which indicates that CAM_{sw} in WRF does not fully account for scattering by aerosols. This physical difference will mask the biases in net long-wave radiation when the CAM_{sw} is used, making it more difficult to identify remaining biases, unless each radiation flux component is treated individually. Comparing CAM_{lw} and $RRTMG_{lw}$ an increase in daytime LW_D bias of 8 W m^{-2} is identified, causing an increase in Q^* bias. The CAM_{lw} aligns with the impact of a decrease in CO_2 concentration. That does not indicate an absence of CO_2 effects on LW_D in CAM_{lw} but is related to a different physical description of long-wave radiation between the schemes and it could originate from not accounting fully for water vapor effects on LW_D and from the few spectral bands used compared to the RRTMG scheme. The exact same biases from CAM_{sw} and CAM_{lw} are seen throughout Figures 3a, 3c, 4a, 4c, 5, and 6 indicating the importance of the radiation scheme choice.

4.2. Boundary Layer Schemes

Changes in atmospheric forcing do not clearly explain daytime deviations between the different boundary layer parameterization schemes used (YSU, QNSE, and the reference MYJ). Although initially ADV_θ appears to be the primary difference between YSU and the other two schemes, this is misleading as advection is the same for all. Changes in CH_{heat} and CH_{mom} cannot explain the variations, neither can changes in CO_2 or AOD. Considering that runs with different boundary layer schemes show small variation in Q^* (Figure 3a), but large variation in ΔT_{50m}, the differences should be primarily driven by the physical description of turbulent processes. Indeed for the daytime the main difference between YSU and MYJ seems to be the explicit inclusion of entrainment of heat in the YSU scheme and a slightly enhanced surface Q_H, potentially due to the different surface layer scheme YSU is coupled to. Moreover, decreasing ADV_θ does produce the same effect as the explicit inclusion of entrainment, because both increase mean boundary layer temperature (consistent with the larger ΔT_{50m} for YSU) and boundary layer height in YSU (not shown). Thus, additional attention should be given not to misinterpret compensating effects from these two physical processes. At night the YSU scheme impact is similar to effects of increased CH_{heat} (Figure 3c). This is expected as increased CH_{heat} indicates stronger nocturnal stability via enhanced radiative cooling due to a stability related feedback mechanism (sections 3.4 and S2.3).

Differences in MYJ and QNSE are minimal for Q^* (Figures 3a and 3c) and the $Q_H/\Delta Q_s$ partitioning (Figures 4a and 4c) at both time periods. However, substantial differences occur between them in ΔT_{50m}

and stability (Figure 6a and 6c). Runs with the QNSE schemes have a smaller diurnal cycle of temperature and instability, reduced buoyancy flux during the day, and weaker stability at night. The nocturnal deviation from MYJ is caused by stronger wind shear in the QNSE schemes, which appears to be related with lower CH_{heat} and CH_{mom} at nighttime that reduce the radiative cooling at the surface.

4.3. Urban Canopy Models

The different model results from SLUCM, BEP + BEM, and BEP model can be explained reasonably well with the surface parameters differences. SLUCM can match the daytime BEP + BEM results reasonably well by decreasing a_{roof} (to 0.12) and a_{kanda} (to 0.80) and increasing C_{wall} (to 1.8*10^6 J m^{-3} K^{-1}). Decreasing the SLUCM a_{roof} is consistent with the lower bulk albedo for the BEP + BEM and BEP models, which have different physical description of the urban morphology and shading. The a_{kanda} change increases the modeled 2 m exchange coefficient of heat for SLUCM, which is lower than in BEP + BEM. The increase in SLUCM C_{wall} increases the ΔQ_s and can compensate the lack of a building energy model and air-conditioning cooling (present in BEP + BEM), which increases the heat capacity of the urban fabric as internal building temperatures remain lower. Exclusion of the BEM module in the multilayer scheme leads to substantially larger Q_H and lower thermal storage. To match BEP with SLUCM in addition to the changes in a_{kanda} and a_{roof} are needed as well as, a decrease in λ_{wall} (to 0.45) and a reduction of Q_f to 0 W m^{-2} (BEP does not account for Q_f).

These modifications reduce the differences between SLUCM, BEP + BEM, and BEP, causing a daytime ΔT_{50m} difference reduction to 0.20°C (from 0.75°C) and a 0.06°C reduction at night (from 0.25°C). Q^* is only improved during the day and becomes identical to BEP + BEM with large reduction in the differences between the SW_U and LW_U between the two schemes. The same is true for $Q_H/\Delta Q_s$ and the Ri_b, which indicates more similarity in the surface fluxes and the near-surface atmospheric stability. However, at night substantial differences remain in Q^*, due to higher skin temperatures in SLUCM and also in $Q_H/\Delta Q_s$ as Q_H in SLUCM is lower compared to BEP + BEM.

5. Discussion

This analysis identifies the model response to changes in atmospheric forcing and urban surface parameter for a specific model configuration (section 2.2) and for a specific UCM (SLUCM). The same sensitivity analysis with different model configurations (e.g., different NWP or reference parameterization schemes) and UCMs are anticipated to lead to different model responses. This is to be expected due to differences in model setups and UCMs. Hence, we recommend other UCMs with more complex (i.e., multilayer schemes) and more simplified (e.g., bulk schemes) physical description of the urban surface to be tested. Similarly different case studies, urban areas, and predominant meteorological conditions (e.g., cloudy/rain period, different geostrophic wind speeds) need to be considered.

To ensure our analysis is not day-specific, we compare the model responses between the first and second days of the SUBLIME case study. During the second day geostrophic wind speed is substantial lower; thus sensitivity of the model's response to geostrophic wind is also tested. The model response remains similar between the 2 days, with the few differences linked to the nonlinear feedback between daytime T_{50m} and nocturnal atmospheric stability, causing nonlinear behavior for some variables due to the generally larger Ri_b during the second day, an effect of the lower wind speeds.

The plausible uncertainty range in atmospheric forcing and surface parameters (as presented in section 2.3) is based on previous reported sensitivity tests and uncertainty estimates (Loridan et al., 2010; Wang et al., 2011; Zhao et al., 2014). It could however undersample or oversample the uncertainty range for specific parameters leading to skewed model sensitivity. It is expected that such an effect would be more profound on the actual range of the sensitivity and not so much on the orientation or linearity of the model's response in the parameter space. However, under low wind conditions the response for some parameters might be nonlinear due to stability effects. Therefore, careful selection for the uncertainty range and the frequency of sampling from the parameter range is essential. For CH_{heat} and CH_{mom}, changes in other atmospheric forcing or surface parameters will affect the calculated values, but their effect is small compared to changes in the multiplication factors.

The 1-D WRF-Noah setup and the boundary layer scheme influence the outcome of the sensitivity analysis. In reality a boundary layer will react differently to changes in physical properties of the underlying surface. For example, any variation in the urban surface temperature over the urban area will likely result in a change of temperature advection and also wind speed due to changes in pressure gradient. Such processes cannot be represented in a 1-D where advection is prescribed but will require 3-D simulations. Such limitations in the representation of the overlying atmosphere might exclude feedback mechanisms that could change the sensitivity reported in this study.

Following Tsiringakis et al. (2019), we used the LW_{up} calculated in the SLUCM rather than the WRF reference as the LW_{up} from the long-wave radiation scheme uses an average aerodynamic surface temperature instead of the radiative skin temperature of the facets. SLUCM calculates this aerodynamic surface temperature diagnostically from the air temperature, Q_H and the modeled exchange coefficient of heat. During our analysis we found that this aerodynamic surface temperature varies substantial from the radiative skin temperature of the urban facets. Since the BEP + BEM and BEP schemes use a similar approach to calculate the LW_{up} (i.e., via the radiative skin temperature) we used the same approach for WRF-SLUCM-Noah. Note that this difference does not affect Q^* at the surface, as this LW_{up} is from the urban scheme, using the radiative temperature.

This study does not optimize the model performance but tries to understand how uncertainty in forcing and parameters affect key physical processes in the urban surface and overlying atmosphere. However, if one is mainly interested in improving model performance through optimization there are a series of potential techniques to do so. Loridan et al. (2010) and Zhao et al. (2014) used ensemble Kalman filtering and Monte Carlo approach to optimize the urban surface parameters in order to improve the SLUCM′ s performance, with very promising results. For offline or even limited 1-D model simulation that might be computationally possible, but for full 3-D model simulations the computational cost might be prohibitive. Inverse modeling with the adjoint model of WRF (Zhang et al., 2013) might be more efficient.

Here we use modeled $\Delta T_{50\mathrm{m}}$ rather than the modeled $T_{50\mathrm{m}}$ (following Sterk et al., 2013) to minimize the impact of biases introduced during spin-up phase and to allow analysis of model response to changes in atmospheric forcing and surface parameters separately for day and night. Thus we are able to easily distinguish compensating effects on $T_{50\mathrm{m}}$ between day and night (e.g., changes in λ_{wall} and CH_{heat}) or carryover effects from day to night (e.g., ADV_{θ} and Q_f). Moreover, the changes in $\Delta T_{50\mathrm{m}}$ during day or night are directly linked with the changes in radiation and surface energy balance. This allows us to identify more accurately, which atmospheric forcing or surface parameter changes explains the bias between model and observations or differences between different model setups.

6. Conclusions

In a coupled NWP-UCM model setup, surface parameters and atmospheric forcing are the primary sources of uncertainty and strongly affect model performance. With WRF-SLUCM-Noah we investigate the impact of these sources during a 1-day clear-skies period in London. The impact of change in atmospheric forcing and surface parameters to the surface radiative balance, energy partitioning, and intensity of turbulent mixing are calculated together with the coupling between the surface and the overlying atmosphere.

Both atmospheric forcing and surface parameters changes impact the model's performance. For the radiative balance, AOD, a_{roof},CO_2, and a_{kanda} are the most influential parameters, each impacting different terms. SW_U and LW_U cause the bias in modeled Q^*. Correcting for the radiative bias improves the radiative heating and radiative cooling performance. For the surface energy flux partitioning, the model has the largest response to changes in CH_{heat},a_{kanda},Q_f,C_{wall}, and λ_{wall}. Changes in near-surface atmospheric stability are comparable in magnitude from most changes in atmospheric forcing and surface parameters, with different orientation for each of the sources. Changes in CH_{heat} have the largest impact on daytime Ri_b, while ADV_{heat}, a_{kanda}, C_{wall} and λ_{wall} are more critical at night. A feedback mechanism between increasing daytime T_{50m} and increase in nocturnal radiative cooling is identified. Its intensity is strongly depended on the wind shear.

We identify some compensating effects between atmospheric forcing and surface parameters changes in this analysis. This is mainly for surface parameters related to thermal storage (e.g., f_{urban}, C_{wall} and λ_{wall}) and

between CH_{heat} and a_{kanda}, which are linked to the surface atmosphere coupling. Both AOD and a_{roof} impacts on Q^* and surface flux partitioning are similar. The reported compensating effects, evident from single variable analysis, are reduced by using the 2-variable space analysis (the so-called the processes diagrams). Various atmospheric forcing and surface parameter changes have similar effects, if not separated by time of day. This supports the Best and Grimmond (2015) suggestion to analyze model responses under different turbulence regimes.

We highlight that it is possible to identify physical description differences between the schemes used in our WRF-SLUCM-Noah setup. This is easier when key physical mechanisms are missing from a scheme (e.g., lack of aerosol effects on SW_D) but is more difficult when the process is not covered by the atmospheric forcing range of analysis (e.g., explicit entrainment flux in YSU compared to MYJ). This analysis can also identify compensating effect between atmospheric processes, as demonstrated by the fact that decreasing ADV_θ shows a similar effect to including explicit entrainment. We could identify differences in the UCM schemes through the use of changes in the surface parameters and link them to differences in the physical complexity of the schemes, which allows to link uncertainty to either changes in atmospheric forcing or surface parameters. However, this approach has clear limitation (e.g., inability to explained the difference in nocturnal Q^* between SLUCM and BEP + BEM).

Appendix A: Definition for Symbols

Table A1
List of Definitions for the Symbols/Abbreviations Used to Define Atmospheric Forcing Components, Surface Parameters, Tested Parameterization Schemes, and Other Relevant Variables

Symbol	Definition
a_{kanda}	Kanda parameter
a_{roof}	Roof albedo
ADV_θ	Advection of potential temperature
ADV_q	Advection of moisture
AOD	Aerosol optical depth
BEP	Building environment parameterisation (Martilli et al., 2002)
$BEP+BEM$	BEP + Building Energy Model (Salamanca & Martilli, 2009)
CAM_{sw}	CAM short-wave radiation scheme (Collins et al., 2004)
CAM_{lw}	CAM long-wave radiation scheme (Collins et al., 2004)
CO_2	Concentration of CO_2 in ppm
CH_{heat}	Exchange coefficient of heat
CH_{mom}	Exchange coefficient of momentum
C_{wall}	Heat capacity of walls
ΔQ_s	Storage heat flux
ΔT_{50m}	Difference between $T_{50m,max}$ and $T_{50m,min}$
ΔT_{skin}	Difference between $T_{skin,max}$ and $T_{skin,min}$
f_{urban}	Urban fraction
λ_{wall}	Thermal conductivity of walls
LW_D	Long-wave downward radiation
LW_U	Long-wave upward radiation
MYJ	Mellor-Yamada-Janjic boundary layer scheme (Janjic, 1994)
Q_f	Anthropogenic heat flux
Q^*	Net all-wave radiation
Q_H	Sensible heat flux
Q_E	Latent heat flux
$QNSE$	Quasinormal Scale Elimination boundary layer scheme (Sukoriansky et al., 2005)
SW_D	Short-wave downward radiation
SW_U	Short-wave upward radiation
$SLUCM$	Single-layer urban canopy model (Kusaka et al., 2001)
YSU	Yonsei university boundary layer scheme (Hong et al., 2006)

Data Availability Statement

The data set for this research (Tsiringakis et al., 2020) is publicly available in the Zenodo repository (https://zenodo.org/record/3897222, doi: 10.5281/zenodo.3897222).

Acknowledgments

This research has been funded by the NWO grant no. 864.14.007. The authors would like to thank the ECMWF for providing operational analysis data, the University of Wyoming for the radio-sounding data, and also NOAA for providing data for the WMO stations, all of which were used to create the forcing for the online model. Moreover, we would like to thank NASA/EOSDIS for providing AOD data via the EOSDIS Worldview site and the various grants that support the London observations (LUMA). Finally, we would like to thank all the co-authors of the SUBLIME case study, which is utilized by this paper.

References

Best, M. J., & Grimmond, C. S. B. (2015). Key conclusions of the first international urban land surface model comparison project. *Bulletin of the American Meteorological Society*, *96*(5), 805–819. https://doi.org/10.1175/BAMS-D-14-00122.1

Best, M. J., & Grimmond, C. S. B. (2016). Investigation of the impact of anthropogenic heat flux within an urban land surface model and PILPS-urban. *Theoretical and Applied Climatology*, *126*(1), 51–60. https://doi.org/10.1007/s00704-015-1554-3

Bohnenstengel, S. I., Evans, S., Clark, P. A., & Belcher, S. E. (2011). Simulations of the London urban heat island. *Quarterly Journal of the Royal Meteorological Society*, *137*(659), 1625–1640. https://doi.org/10.1002/qj.855

Bohnenstengel, S. I., Hamilton, I., Davies, M., & Belcher, S. E. (2014). Impact of anthropogenic heat emissions on London's temperatures. *Quarterly Journal of the Royal Meteorological Society*, *140*(679), 687–698. https://doi.org/10.1002/qj.2144

Bosveld, F. C., Baas, P., Steeneveld, G.-J., Holtslag, A. A. M., Angevine, W. M., Bazile, E., et al. (2014). The third GABLS intercomparison case for evaluation studies of boundary-layer models. Part B: Results and process understanding. *Boundary-Layer Meteorology*, *152*(2), 157–187. https://doi.org/10.1007/s10546-014-9919-1

Chen, F., & Dudhia, J. (2001). Coupling an advanced land surface–hydrology model with the Penn State NCAR MM5 modeling system. Part I: Model implementation and sensitivity. *Monthly Weather Review*, *129*(4), 569–585. https://doi.org/10.1175/1520-0493(2001) 129<0569:CAALSH>2.0.CO;2

Chen, F., Kusaka, H., Bornstein, R., Ching, J., Grimmond, C. S. B., Grossman-Clarke, S., et al. (2011). The integrated WRF/urban modelling system: Development, evaluation, and applications to urban environmental problems. *International Journal of Climatology*, *31*(2), 273–288. https://doi.org/10.1002/joc.2158

Collins, W., Rasch, P., & Coauthors (2004). Description of the NCAR community atmosphere model (CAM 3.0). (Ncar Tech. note ncar/tn464+str). 214 pp.

Demuzere, M., Harshan, S., Jrvi, L., Roth, M., Grimmond, C. S. B., Masson, V., et al. (2017). Impact of urban canopy models and external parameters on the modelled urban energy balance in a tropical city. *Quarterly Journal of the Royal Meteorological Society*, *143*(704), 1581–1596. https://doi.org/10.1002/qj.3028

Dong, Y., Varquez, A. C. G., & Kanda, M. (2017). Global anthropogenic heat flux database with high spatial resolution. *Atmospheric Environment*, *150*, 276–294. https://doi.org/10.1016/j.atmosenv.2016.11.040

ECMWF (2012). Atmospheric model high resolution 10-day forecast (HRES). https://www.ecmwf.int/en/forecasts/datasets/set-i (accessed: 18-04-2017).

Ferrero, E., Alessandrini, S., & Vandenberghe, F. (2018). Assessment of planetary-boundary-layer schemes in the weather research and forecasting model within and above an urban canopy layer. *Boundary-Layer Meteorology*, *168*(2), 289–319. https://doi.org/10.1007/s10546-018-0349-3

Gomes, L., Mallet, M., Roger, J. C., & Dubuisson, P. (2008). Effects of the physical and optical properties of urban aerosols measured during the capitoul summer campaign on the local direct radiative forcing. *Meteorology and Atmospheric Physics*, *102*(3), 289. https://doi.org/10.1007/s00703-008-0321-8

Grimmond, C. S. B., Blackett, M., Best, M. J., Baik, J.-J., Belcher, S. E., Beringer, J., et al. (2011). Initial results from Phase 2 of the international urban energy balance model comparison. *International Journal of Climatology*, *31*(2), 244–272. https://doi.org/10.1002/joc.2227

Grimmond, C. S. B., Blackett, M., Best, M. J., Barlow, J., Baik, J.-J., Belcher, S. E., et al. (2010). The international urban energy balance models comparison project: First results from phase 1. *Journal of Applied Meteorology and Climatology*, *49*(6), 1268–1292. https://doi.org/10.1175/2010JAMC2354.1

Grimmond, C. S. B., & Oke, T. R. (1991). An evapotranspiration-interception model for urban areas. *Water Resources Research*, *27*(7), 1739–1755. https://doi.org/10.1029/91WR00557

Grimmond, C. S. B., & Oke, T. R. (1999). Heat storage in urban areas: Local-scale observations and evaluation of a simple model. *Journal of Applied Meteorology*, *38*(7), 922–940. https://doi.org/10.1175/1520-0450(1999)038<0922:HSIUAL>2.0.CO;2

Heaviside, C., Cai, X.-M., & Vardoulakis, S. (2015). The effects of horizontal advection on the urban heat island in Birmingham and the West Midlands, United Kingdom during a heatwave. *Quarterly Journal of the Royal Meteorological Society*, *141*(689), 1429–1441. https://doi.org/10.1002/qj.2452

Hong, S.-Y., Dudhia, J., & Chen, S.-H. (2004). A revised approach to ice microphysical processes for the bulk parameterization of clouds and precipitation. *Monthly Weather Review*, *132*(1), 103–120. https://doi.org/10.1175/1520-0493(2004)132<0103:ARATIM>2.0.CO;2

Hong, S.-Y., Noh, Y., & Dudhia, J. (2006). A new vertical diffusion package with an explicit treatment of entrainment processes. *Monthly Weather Review*, *134*(9), 2318–2341. https://doi.org/10.1175/MWR3199.1

Iacono, M. J., Delamere, J. S., Mlawer, E. J., Shephard, M. W., Clough, S. A., & Collins, W. D. (2008). Radiative forcing by long-lived greenhouse gases: Calculations with the AER radiative transfer models. *Journal of Geophysical Research*, *113*, D13103. https://doi.org/10.1029/2008JD009944

Iamarino, M., Beevers, S., & Grimmond, C. S. B. (2012). High-resolution (space, time) anthropogenic heat emissions: London 19702025. *International Journal of Climatology*, *32*(11), 1754–1767. https://doi.org/10.1002/joc.2390

Janjic, Z. I. (1994). The step-mountain eta coordinate model: Further developments of the convection, viscous sublayer, and turbulence closure schemes. *Monthly Weather Review*, *122*(5), 927–945. https://doi.org/10.1175/1520-0493(1994)122<0927:TSMECM>2.0.CO;2

Jarvi, L., Grimmond, C. S. B., & Christen, A. (2011). The surface urban energy and water balance scheme (SUEWS): Evaluation in Los Angeles and Vancouver. *Journal of Hydrology*, *411*(3), 219–237. https://doi.org/10.1016/j.jhydrol.2011.10.001

Kanda, M., Kanega, M., Kawai, T., Moriwaki, R., & Sugawara, H. (2007). Roughness lengths for momentum and heat derived from outdoor urban scale models. *Journal of Applied Meteorology and Climatology*, *46*(7), 1067–1079. https://doi.org/10.1175/JAM2500.1

Kleczek, M. A., Steeneveld, G.-J., & Holtslag, A. A. M. (2014). Evaluation of the weather research and forecasting mesoscale model for GABLS3: Impact of boundary-layer schemes, boundary conditions and spin-up. *Boundary-Layer Meteorology*, *152*(2), 213–243. https://doi.org/10.1007/s10546-014-9925-3

Kokkonen, T. V., Grimmond, S., Murto, S., Liu, H., Sundström, A.-M., & Järvi, L. (2019). Simulation of the radiative effect of haze on the urban hydrological cycle using reanalysis data in Beijing. *Atmospheric Chemistry and Physics*, *19*(10), 7001–7017. https://doi.org/10.5194/acp-19-7001-2019

Kotthaus, S., & Grimmond, C. S. B. (2014a). Energy exchange in a dense urban environment - Part I: Temporal variability of long-term observations in central London. *Urban Climate*, *10*(P2), 261–280. https://doi.org/10.1016/j.uclim.2013.10.002

Kotthaus, S., & Grimmond, C. S. B. (2014b). Energy exchange in a dense urban environment - Part II: Impact of spatial heterogeneity of the surface. *Urban Climate*, *10*(P2), 281–307. https://doi.org/10.1016/j.uclim.2013.10.001

Kusaka, H., Kondo, H., Kikegawa, Y., & Kimura, F. (2001). A simple single-layer urban canopy model for atmospheric models: Comparison with multi-layer and slab models. *Boundary-Layer Meteorology*, *101*(3), 329–358. https://doi.org/10.1023/A:1019207923078

Levy, R. C., Mattoo, S., Munchak, L. A., Remer, L. A., Sayer, A. M., Patadia, F., & Hsu, N. C. (2013). The collection 6 MODIS aerosol products over land and ocean. *Atmospheric Measurement Techniques*, *6*(11), 2989–3034. https://doi.org/10.5194/amt-6-2989-2013

Lindberg, F., Grimmond, C. S. B., Yogeswaran, N., Kotthaus, S., & Allen, L. (2013). Impact of city changes and weather on anthropogenic heat flux in Europe 1995–2015. *Urban Climate*, *4*, 1–15. https://doi.org/10.1016/j.uclim.2013.03.002

Loridan, T., & Grimmond, C. S. B. (2012). Multi-site evaluation of an urban land-surface model: Intra-urban heterogeneity, seasonality and parameter complexity requirements. *Quarterly Journal of the Royal Meteorological Society*, *138*(665), 1094–1113. https://doi.org/10.1002/qj.963

Loridan, T., Grimmond, C. S. B., Grossman-Clarke, S., Chen, F., Tewari, M., Manning, K., et al. (2010). Trade-offs and responsiveness of the single-layer urban canopy parametrization in WRF: An offline evaluation using the MOSCEM optimization algorithm and field observations. *Quarterly Journal of the Royal Meteorological Society*, *136*(649), 997–1019. https://doi.org/10.1002/qj.614

Martilli, A., Clappier, A., & Rotach, M. W. (2002). An urban surface exchange parameterisation for mesoscale models. *Boundary-Layer Meteorology*, *104*(2), 261–304. https://doi.org/10.1023/A:1016099921195

Masson, V. (2000). A physically-based scheme for the urban energy budget in atmospheric models. *Boundary-Layer Meteorology*, *94*(3), 357–397. https://doi.org/10.1023/A:1002463829265

NASA/EOSDIS (2019). NASA worldview. https://worldview.earthdata.nasa.gov (accessed:01-08-2019)

NOAA/NCDC (2012). Climate sata online. https://www.ncdc.noaa.gov/cdo-web/datasets (accessed:30-06-2017)

Oikonomou, E., Davies, M., Mavrogianni, A., Biddulph, P., Wilkinson, P., & Kolokotroni, M. (2012). Modelling the relative importance of the urban heat island and the thermal quality of dwellings for overheating in London. *Building and Environment*, *57*, 223–238. https://doi.org/10.1016/j.buildenv.2012.04.002

Powers, J. G., Klemp, J. B., Skamarock, W. C., Davis, C. A., Dudhia, J., Gill, D. O., et al. (2017). The weather research and forecasting model: Overview, system efforts, and future directions. *Bulletin of the American Meteorological Society*, *98*(8), 1717–1737. https://doi.org/10.1175/BAMS-D-15-00308.1

Ronda, R. J., Steeneveld, G. J., Heusinkveld, B. G., Attema, J. J., & Holtslag, A. A. M. (2017). Urban finescale forecasting reveals weather conditions with unprecedented detail. *Bulletin of the American Meteorological Society*, *98*(12), 2675–2688. https://doi.org/10.1175/BAMS-D-16-0297.1

Salamanca, F., & Martilli, A. (2009). A new building energy model coupled with an urban canopy parameterization for urban climate simulations—Part II. Validation with one dimension off-line simulations. *Theoretical and Applied Climatology*, *99*(3), 345. https://doi.org/10.1007/s00704-009-0143-8

Schmid, H. P., Cleugh, H. A., Grimmond, C. S. B., & Oke, T. R. (1991). Spatial variability of energy fluxes in suburban terrain. *Boundary-Layer Meteorology*, *54*(3), 249–276. https://doi.org/10.1007/BF00183956

Skamarock, W. C., Klemp, J. B., Dudhia, J., Gill, D. O., Barker, D. M., Wang, W., & Powers, J. G. (2008). A description of the advanced research WRF version 3. NCAR Technical note -475+STR.

Steeneveld, G.-J., Tsiringakis, A., Barlow, J., Bohnenstengel, S. I., Grimmond, C. S. B., Halios, C., et al. (2017). Single-column urban boundary layer inter-comparison modelling experiment (SUBLIME): Call for participation. *Urban Climate News*, *66*, 21–26.

Sterk, H. A. M., Steeneveld, G. J., & Holtslag, A. A. M. (2013). The role of snow-surface coupling, radiation, and turbulent mixing in modeling a stable boundary layer over arctic sea ice. *Journal of Geophysical Research: Atmospheres*, *118*, 1199–1217. https://doi.org/10.1002/jgrd.50158

Sukoriansky, S., Galperin, B., & Perov, V. (2005). Application of a new spectral theory of stably stratified turbulence to the atmospheric boundary layer over sea ice. *Boundary-Layer Meteorology*, *117*(2), 231–257. https://doi.org/10.1007/s10546-004-6848-4

Tsiringakis, A., Holtslag, A. A. M., Grimmond, S., & Steeneveld, G. J. (2020). Model and observational dataset used in Tsiringakis, A., Holtslag, A.A.M., Grimmond, S. and Steeneveld, G.J. Surface and atmospheric driven variability of the single-layer urban canopy model under clear sky conditions over London, Journal of Geophysical Research: Atmospheres. *Zenodo*. https://doi.org/10.5281/zenodo.3897222

Tsiringakis, A., Steeneveld, G. J., Holtslag, A. M., Kotthaus, S., & Grimmond, C. S. B. (2019). On- and off-line evaluation of the single-layer urban canopy model in london summertime conditions. *Quarterly Journal of the Royal Meteorological Society*, *145*(721), 1474–1489. https://doi.org/10.1002/qj.3505

UWYO (2012). Atmospheric soundings. http://weather.uwyo.edu/upperair/sounding.html (accessed:20-04-2017)

Wang, Z.-H., Bou-Zeid, E., Au, S. K., & Smith, J. A. (2011). Analyzing the sensitivity of WRF's single-layer urban canopy model to parameter uncertainty using advanced Monte Carlo simulation. *Journal of Applied Meteorology and Climatology*, *50*(9), 1795–1814. https://doi.org/10.1175/2011JAMC2685.1

Ward, H. C., Kotthaus, S., Jrvi, L., & Grimmond, C. S. B. (2016). Surface urban energy and water balance scheme (SUEWS): Development and evaluation at two uk sites. *Urban Climate*, *18*, 1–32. https://doi.org/10.1016/j.uclim.2016.05.001

Zhang, X., Huang, X.-Y., & Pan, N. (2013). Development of the upgraded tangent linear and adjoint of the Weather Research and Forecasting (WRF) model. *Journal of Atmospheric and Oceanic Technology*, *30*(6), 1180–1188. https://doi.org/10.1175/jtech-d-12-00213.1

Zhao, W., Zhang, N., Sun, J., & Zou, J. (2014). Evaluation and parameter-sensitivity study of a single-layer urban canopy model (SLUCM) with measurements in Nanjing China. *Journal of Hydrometeorology*, *15*(3), 1078–1090. https://doi.org/10.1175/JHM-D-13-0129.1